Available online at www.sciencedirect.com
ScienceDirect
International Journal of Heat and Fluid Flow 29 (2008) 783–791
International Journal of HEAT AND FLUID FLOW
www.elsevier.com/locate/ijhff

Drag reduction by dimples? – A complementary experimental/numerical investigation

Hermann Lienhart, Michael Breuer *, Cagatay Köksoy

Institute of Fluid Mechanics, University of Erlangen-Nürnberg, Cauerstrasse 4, D-91058 Erlangen, Germany

Received 30 October 2007; received in revised form 28 January 2008; accepted 1 February 2008
Available online 24 March 2008

Abstract

The paper is concerned with an experimental and numerical investigation of the turbulent flow over dimpled surfaces. Shallow dimples distributed regularly over the wall of a plane channel with large aspect ratio are used to study their effect on the friction drag. The resulting pressure drop in the channel was measured for smooth and dimpled walls. In addition to these investigations on internal flows, an external flow study was performed and boundary-layer profiles were measured using a Pitot-tube rake. Complementary to the measurements, direct numerical simulations for the internal flow configuration with and without dimples were carried out for two different grid resolutions and analyzed in detail. The objective was to clarify whether or not dimples cause reduction of the skin-friction drag.

PACS: 47.85.Ib; 47.80.Fg; 47.27.ek; 47.27.nd

Keywords: Dimples; Drag reduction; Skin-friction drag; Measurements; Direct numerical simulation (DNS)

1. Introduction

Introducing a regular arrangement of surface depressions called *dimples* is a well-known measure to increase heat-transfer from a wall. Compared to a smooth wall, the Nusselt number can be significantly enhanced by dimples, whereas the increase of the pressure drop was found to be small. For that purpose, deep dimples with a ratio of depth to print diameter of $h/D = 0.2$–0.5 are typically applied to enhance the convective transport from the wall (see e.g., Burgess et al., 2003).

Some years back Russian scientists (see e.g., Alekseev et al., 1998) discovered that apart from heat-transfer enhancement dimples might be useful for drag reduction. Their findings are based on experimental measurements of turbulent flows over surfaces with a regular arrangement of *shallow* dimples leading to a decrease of the skin-friction drag of a turbulent flow up to 20%. (Note that this is not the "golf ball" effect!) However, up to now no clear explanation has been provided which can illuminate this effect. Hence some doubts remain regarding the experimental investigations and their outcome. Compared to classical devices for drag reduction, such as riblets, shallow dimples would be advantageous since they are composed of macroscopic structures which are less sensitive to dirt and mechanical degradation. Furthermore, their effectiveness should not depend on the flow direction.

Since the drag reduction promised by dimples would have a tremendous economical influence, it is worth studying it in more detail. For that purpose, experimental investigations as well as direct numerical simulations (DNS) of the turbulent flow inside a channel with dimpled walls were carried out to investigate the physical mechanism. As the reference test case the fully developed turbulent channel flow was chosen because it offers several significant advantages: there are no other drag components involved but skin-friction, the boundary conditions are very well defined

* Corresponding author.
E-mail addresses: lienhart@lstm.uni-erlangen.de (H. Lienhart), mbreuer@lstm.uni-erlangen.de (M. Breuer), ckoeksoy@lstm.uni-erlangen.de (C. Köksoy).

0142-727X/$ - see front matter © 2008 Elsevier Inc. All rights reserved.
doi:10.1016/j.ijheatfluidflow.2008.02.001

and the wall-shear stress can be deduced from relatively simple and reliable pressure drop measurements. In order to verify the findings of the internal flow tests, some complementary measurements in a zero-pressure-gradient boundary-layer were made, using a Pitot-tube rake.

2. Experimental set-up

2.1. Internal flow

The experimental investigation for internal flows was performed in the channel test rig sketched in Fig. 1. It consisted of the blower/settling chamber unit, the channel test section with exchangeable walls and the measuring instrumentation. The air flow was provided by a centrifugal blower, and the flow rate was varied by means of a closed-loop rpm control unit. The settling chamber was equipped with honeycomb flow straighteners and screens, thus ensuring well-defined flow conditions. The dimensions of the test section in terms of channel height H, width W, and length L were set to 50 mm × 600 mm × 6000 mm. Hence, they were chosen in such a way that two-dimensionality and fully developed state of the channel flow was assured, i.e., the aspect ratio of the channel W/H was 12, and the length over height ratio L/H was 120. In order to accelerate the evolution to the fully developed state, a trip was introduced at the channel inlet. The walls of the channel were constructed from aluminum and the plates with the dimples from poly-acrylic. Two geometries of dimples were tested, both supplied by Inventors Network GmbH, the holder of the patents and representative of the Russian scientists. Most of the results reported in the following refer to the smaller dimple geometry, which was provided as the first choice. The print diameter of these smaller dimples was $D = 15$ mm and the depth $h = 0.75$ mm, while the bigger dimples were machined to $D = 47$ mm and $h = 2$ mm. Both types were arranged in a regular pattern on one channel wall as shown below. The dimples were milled by a numerically controlled machine and the surface was re-polished subsequently (see Fig. 2).

The flow rate, and thus the bulk velocity, was measured using an inlet contraction in front of the blower. Density and viscosity of the air were derived from ambient pressure and temperature. The pressure instrumentation consisted of a Scanivalve unit and a Validyne differential pressure gauge. For each test Reynolds number $Re = U_b\delta/\nu$ (bulk velocity U_b, channel half-width δ) the pressure gradient dp/dx was deduced by a linear fit of the measured pressure data, as shown for a typical example in Fig. 3.

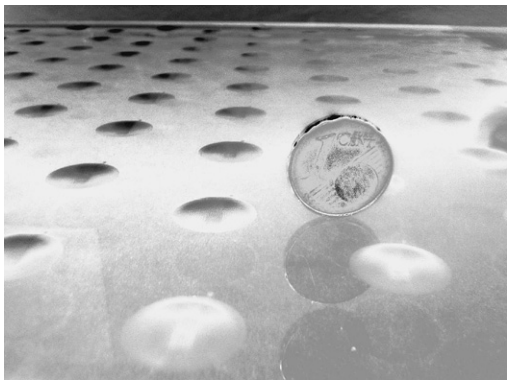

Fig. 2. Plate with milled dimples.

The location and dimensions of the pressure taps are given in Fig. 4. At each x-position there were three pressure taps installed which allowed, prior to the final tests, to

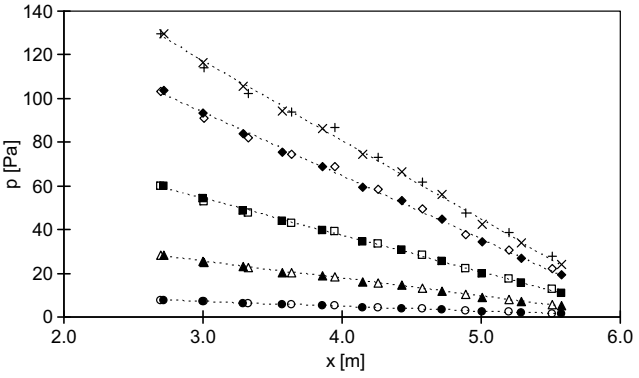

Fig. 3. Pressure distribution measured along flat and dimpled side of the channel for various Reynolds numbers.

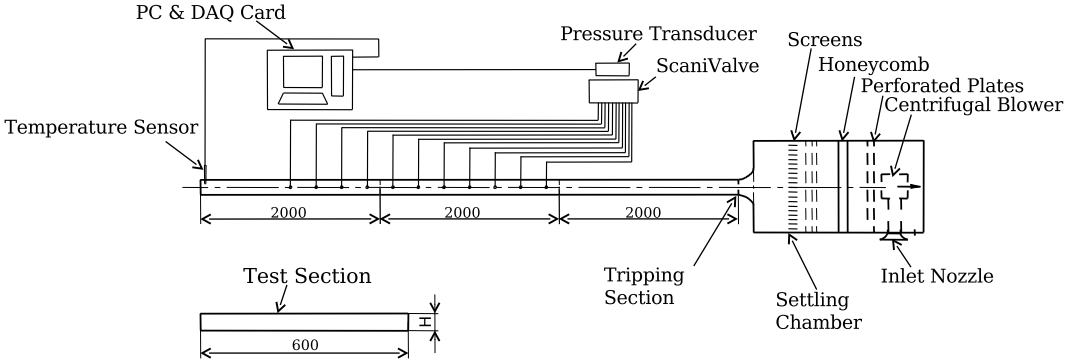

Fig. 1. Experimental set-up of the plane channel flow (units in mm).

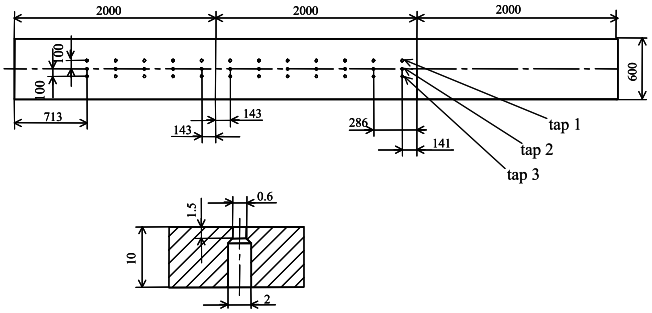

Fig. 4. Location of the pressure taps on the channel.

check the consistency of the readings as well as the two-dimensionality of the flow.

Based on the pressure gradient, the wall-shear stress τ_w and the skin-friction coefficient C_f can be determined according to

$$\tau_w = -\frac{H}{2}\frac{dp}{dx}, \tag{1}$$

$$C_f = \frac{\tau_w}{(1/2)\rho U_b^2}, \tag{2}$$

where ρ denotes the density of the fluid.

2.2. External flow

The external flow study was performed in the open test section closed-loop wind tunnel of LSTM Erlangen. The test section of the tunnel was $1.87 \times 1.4\ m^2$ in cross-section and the turbulence level of the flow was measured to be less than 0.3%.

The test plate was mounted vertically in the test section of the wind tunnel and its orientation relative to the flow was adjusted so that the pressure taps that were placed at the locations A and B, as sketched in Fig. 5, gave identical values. In this way it was ensured that zero-pressure-gradient was achieved along the plate surface. The width of the plate is wide enough, 1.24 m, to guarantee that the three-dimensional flow at the edges of the plate do not propagate and disturb the boundary layer in the center plane of the plate, where the measurements were performed.

Boundary-layer velocity profiles were measured using the Pitot-tube rake depicted in Fig. 6, which was constructed according to the recommendations given in Bui et al. (2000). By using the geometrically fixed rake arrangement mounted directly to the plate surface any additional positioning uncertainties in the y-direction were avoided. The pressure readings of the rake were acquired by a Baratron Type 698A high-accuracy pressure transducer and a 670B signal conditioner. Switching between the individual Pitot-tubes was performed by means of a computer controlled Scanivalve.

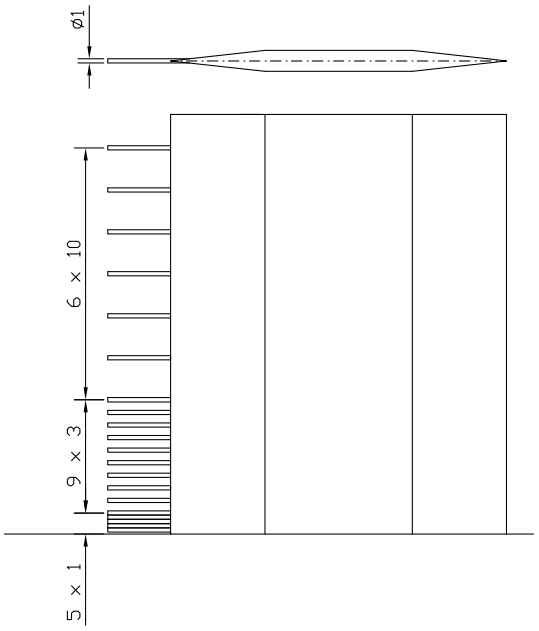

Fig. 6. Sketch of the boundary-layer rake used in the experiment.

The smooth plate measurements performed for comparison were carried out by covering the dimpled plate with a 1 mm stainless steel sheet. Covering the plate instead of exchanging the dimpled plate with a smooth one eliminates any relative positioning errors and errors in pressure-gradient measurements.

Using the Pitot-tube rake the velocity profiles in the front and rear part of the test plate were measured at locations A and B. Three measurement locations were placed in the spanwise direction to consider three-dimensional effects. Based on these data the momentum thickness Θ of the boundary-layer was calculated and the skin-friction coefficients C_f were deduced according to

$$\Theta = \int_0^\infty \frac{U}{U_\infty}\left(1 - \frac{U}{U_\infty}\right)dy, \tag{3}$$

$$C_f = \frac{\Theta_B - \Theta_A}{x_B - x_A}, \tag{4}$$

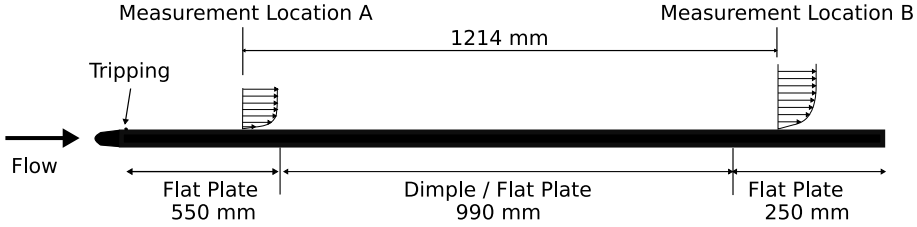

Fig. 5. Experimental set-up of external flow measurements.

where x_A and x_B denote the streamwise position of locations A and B, respectively. For the integration the trapezoidal rule was applied and the momentum losses were averaged over the three measuring positions in the spanwise direction.

3. Direct numerical simulations

3.1. Numerical methodology

The direct numerical simulations were carried out with the CFD code $\mathcal{LESOCC}$ which was developed for the simulation of complex turbulent flows using either the methodology of DNS, large-eddy simulation (LES), or hybrid LES-RANS coupling. $\mathcal{LESOCC}$ is based on a 3-D finite-volume method for arbitrary non-orthogonal and non-staggered, block-structured grids (Breuer and Rodi, 1996; Breuer, 1998, 2002). The spatial discretization of all fluxes is based on central differences of second-order accuracy. A low-storage multi-stage Runge–Kutta method (second-order accurate) is applied for time-marching. In order to ensure the coupling of pressure and velocity fields on non-staggered grids, the momentum interpolation technique is used. $\mathcal{LESOCC}$ is highly vectorized (>99.8%) and additionally parallelized by domain decomposition using MPI. The present simulations were carried out on the NEC SX-8 machine at HLRS Stuttgart using eight processors of one node leading to a total performance of about 52.7 GFlop/s.

3.2. Description of the configurations

In order to investigate the effect of dimples, a classical wall-bounded flow often studied in literature was considered, i.e., a turbulent plane channel flow at $Re = U_b\delta/\nu = 10,935$ or $Re_\tau = 590$. This test case has several advantages. With smooth non-dimpled walls the flow is homogeneous in streamwise and spanwise directions. This allows to use periodic boundary conditions in both directions and thus avoids the definition of appropriate inflow and outflow boundary conditions. The pressure gradient in the streamwise direction was adjusted such that a fixed mass flow rate ($U_b = \text{const.}$) was assured. Furthermore, no-slip boundary conditions were used at both walls.

Since the simulation cannot cover the entire experimental set-up, the computational domain consisted of a cutout of the channel as sketched in Fig. 7 maintaining periodic boundary conditions in the streamwise and spanwise directions. The lengths of the domain were $4.1744\delta \times 2\delta \times 2.4096\delta$, while all geometrical quantities are scaled by the channel half-width $\delta = H/2$. Three cases were considered:

- **L**: Plane channel with multiple dimples at the **L**ower wall.
- **B**: Plane channel with multiple dimples at **B**oth walls.
- **R**: Plane channel without dimples, i.e., **R**eference case with smooth walls.

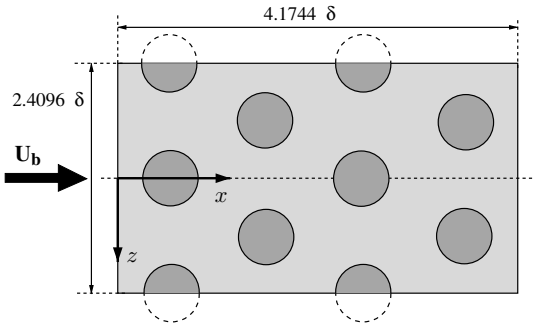

Fig. 7. 2-D sketch (x–z-plane) of the channel with multiple shallow dimples at the wall.

As shown in Fig. 7, multiple shallow dimples (depth to print diameter of $h/D = 0.05$; $D/\delta = 0.6$, dimensions according to those of the small dimples used in the experiments) were arranged regularly on the surface of the lower and/or upper channel walls.

Using block-structured curvilinear grids, two different grid resolutions were taken into account for the DNS (see Table 1). The first, denoted *coarse grid*, consisted of about 5.5 million control volumes (CVs) and thus was not really coarse. For the plane channel case the grid was Cartesian with equidistant grid spacing in streamwise and spanwise directions and a stretched distribution towards both walls according to a geometric series. However, the expansion factor of the geometric series was mild ($r = 1.04$) and the first node was located at a dimensionless distance of $\Delta y^+_{\min} = 0.587$. Hence several grid points were found in the viscous sublayer and the resolution in the homogeneous direction expressed in wall coordinates was of the order $\mathcal{O}(10)$. For the cases with dimples the grid was clinging to the curvilinear geometry of the walls and thus was locally no longer Cartesian.

For the second grid, denoted *fine grid*, the number of control volumes was exactly doubled in each direction for the computational domain sketched in Fig. 7, but due to some extra cells required for the periodic boundary conditions, the numbers given in Table 1 are not exactly doubled. In total about 43 million CVs were used and the resolution in each direction was halved, revealed by the values for Δx^+, $\Delta y^+_{\min}$, and Δz^+ summarized in Table 1. The dimensionless time step sizes were $\Delta t = 4.2 \times 10^{-3}$ and

Table 1
Overview on simulation parameters for the five simulations carried out

Parameter	Coarse grid	Fine grid
Resolution (# CVs)	$260 \times 160 \times 132$	$516 \times 320 \times 260$
$\Delta y_{\min}/\delta$	10^{-3}	5×10^{-4}
Expansion ratio r	1.040	1.023
Δx^+	9.58	4.79
$\Delta y^+_{\min}$	0.587	0.293
Δz^+	11.05	5.52
Δt	4.2×10^{-3}	1.6×10^{-3}
Cases considered	**L**, **B**, **R**	**B**, **R**

$\Delta t = 1.6 \times 10^{-3}$ for the coarse and fine grid, respectively. To achieve reliable statistical data, the flow was averaged over dimensionless time intervals of up to $T_{avg} = 1900$ and 17,000 for the fine and the coarse grid, respectively, which was equivalent to about 450 and 4000 flow-through times (based on the bulk velocity and the channel length). The extremely long averaging time in case of the coarse grid was chosen to verify that the statistics were sufficiently converged after about 400 flow-through times.

4. Results

The skin-friction coefficients measured in the channel flow were plotted as a function of the Reynolds number. Fig. 8 presents a summary of the experimental results for the smaller dimples derived from the pressure gradients displayed in Fig. 3 together with data points derived from integration of the numerically obtained wall quantities. For comparison, data available in the literature (Dean, 1978; Moser et al., 1999) was added. The experimental skin-friction coefficients for the channel flow with smooth walls and with a dimpled wall on one side almost collapse. They differ by less than 1% through all the Reynolds number range considered. Therefore, it may be concluded that, surprisingly, the dimpled wall did not show any increase in pressure loss, but a significant decrease could also not be detected.

Because of this undecided outcome, a different dimple geometry was additionally tested, which was of about three times in size (big dimple). However, this geometry performed worse and resulted in a definite increase of the pressure loss in the channel flow (not shown here).

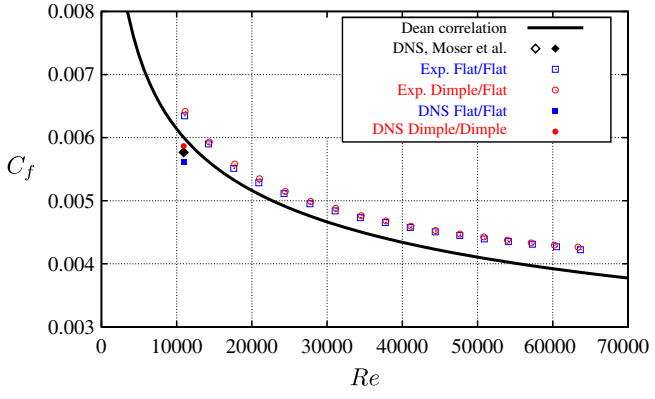

Fig. 8. Measured and predicted friction coefficient C_f vs. Re for different configurations (small dimples); reference data: Dean correlation (Dean, 1978) for plane channel with smooth wall and a large aspect ratio ensuring a 2-D flow, $C_f = 0.06138 \times Re^{-1/4}$ and DNS by Moser et al. (1999).

Table 2
Skin-friction coefficients deduced from the external flow measurements

U	6 m/s	12 m/s
$\frac{C_f^{dimple} - C_f^{smooth}}{C_f^{smooth}}$	−0.38%	2.02%

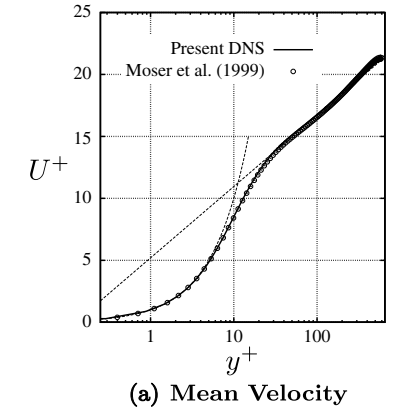

(a) Mean Velocity

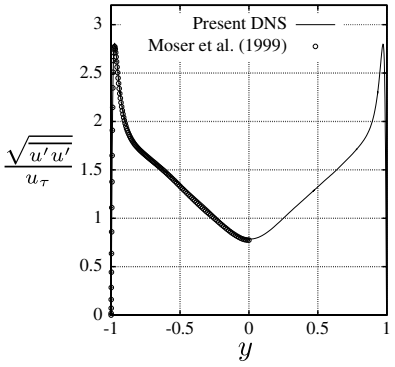

(b) Normal Stress $\overline{u'u'}$

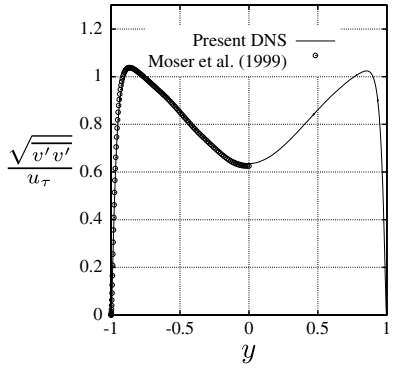

(c) Normal Stress $\overline{v'v'}$

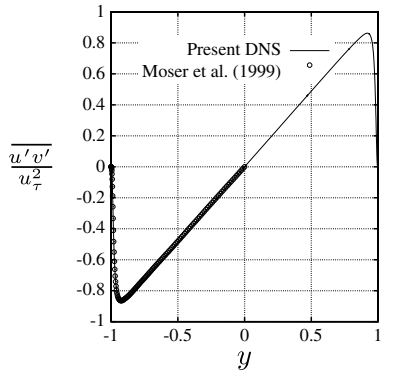

(d) Shear Stress $\overline{u'v'}$

Fig. 9. Channel flow without dimples, case **R**, $Re = 10,935$, comparison of present DNS predictions with DNS data by Moser et al. (1999).

Arguments brought forward by the inventors of the dimpled surfaces reasoned that the claimed effect of drag reduction is achieved by an interaction between the boundary-layer flow in wall vicinity and the outer flow, which is essentially non-viscous. In order to check this objection, an additional external flow test case was set-up, the zero-pressure-gradient flat plate boundary-layer flow described in Section 2.2. Measurements were taken for a plate with the small dimples at three flow velocities: $U = 6$ m/s, 12 m/s, and 24 m/s. At the highest velocity tested, the boundary-layer thickness was too small to be processed to reliable integral results. Therefore, Table 2 summarizes the differences in the skin-friction coefficient between the smooth and the dimpled surface at the two smaller velocities. The quantities displayed have to be considered to lie within the margins of the measurement uncertainties. This again supports the conclusion drawn from the channel flow experiments, namely, that the dimples did not influence drag, neither to the better nor to the worse.

More insight into this not very satisfactory result regarding the integral behavior of the dimpled surface compared to the flat walls was sought using CFD. Since only minor deviations were found between the results obtained on the coarse and the fine grid, in the following only the latter are discussed.

First the quality of the results was checked by comparison of the present predictions with the well-known DNS data by Moser et al. (1999) for the plane channel flow. Fig. 9 depicts the distribution of the mean velocity, the normal Reynolds stresses $\overline{u'u'}$ and $\overline{v'v'}$, and the shear stress component $\overline{u'v'}$. For all quantities shown (and also those not shown here) excellent agreement is found between the present and Moser et al.'s DNS. This points to the high quality of the present DNS.

Fig. 10 depicts results obtained for the case **B** using a regular arrangement of shallow dimples as shown in Fig. 7 on both walls. The time-averaged pressure distribution is shown in Fig. 10a. The influence of the dimples on the pressure distribution on the lower wall can clearly be seen. It should be mentioned that the linear pressure gradient in the streamwise direction of the channel is not included in the figure. In Fig. 10b, the time-averaged

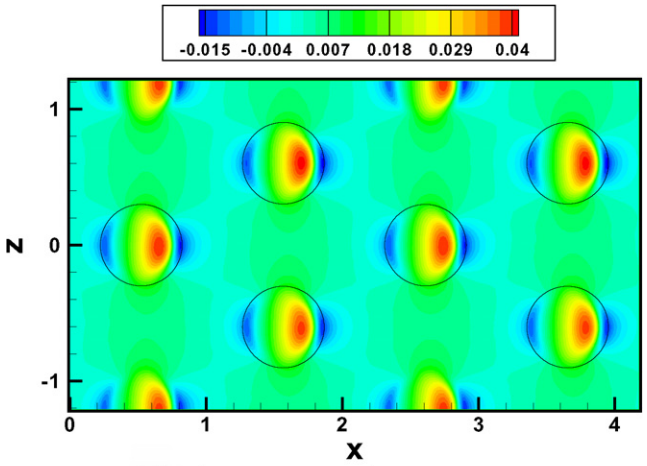

Fig. 10. Channel flow with multiple dimples at both walls, case **B**, fine grid simulation, $Re = 10,935$.

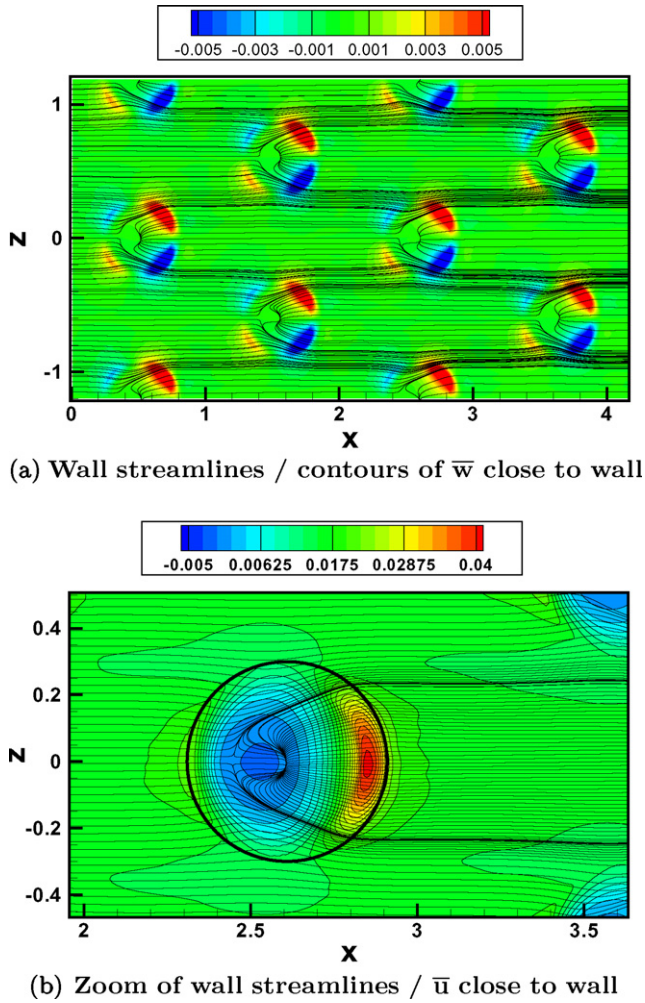

Fig. 11. Channel flow with multiple dimples at both walls, case **B**, fine grid simulation, $Re = 10,935$.

wall-shear stress distribution is displayed. Obviously the wall-shear stresses decrease within the dimples, leading to a very small recirculation region at the falling edge (see Fig. 11). However, at the downstream edge of the dimples, where the fluid flow leaves the surface depression again, large values of the wall-shear stress are found.

In Fig. 11 the streamlines at the lower walls defined by the average surface shear stress are displayed in conjunction with the distribution of the time-averaged spanwise ($\overline{w}$) and streamwise ($\overline{u}$) velocities close to the wall. Upstream of the dimple and partially also in the dimple the streamlines converge. A tiny recirculation region with negative values of $\overline{u}$ visible in Fig. 11b is found inside the dimple. The existence of this phenomenon is confirmed by the results on both grids. At the side and downstream of the recirculation region the streamlines diverge again.

Figs. 12a and b display the time–averaged flow in a x–y midplane of one dimple. Based on the velocity vectors the reduction of the velocity gradient near the wall and thus of the wall-shear stress is visible. On the other hand, it is obvious that the dimples lead to a modified pressure distribution compared with the case of a smooth wall. At both upstream and downstream regions of the dimple, where the flow either enters or leaves the surface depression, the pressure is slightly decreased. However, more important is the observation that the pressure increases on the rising edge of the dimple yielding a contribution to the overall drag, as will be shown below. The strongest flow structures in the time-averaged flow, visualized by iso-surfaces of $\lambda_2 = -0.05$ (normalized by U_b and δ) used as a structure-identification method proposed by Jeong and Hussain (1995) are located at the upstream and downstream edges of the dimple, where the flow enters and leaves the dimple.

Finally, Fig. 13 depicts histories of the forces non-dimensionalized by $\rho U_b^2 \delta^2$ acting on the lower dimpled

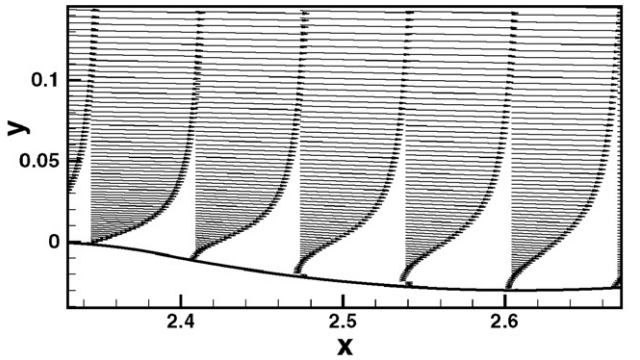

(a) Zoom of the dimple region in a x-y midplane

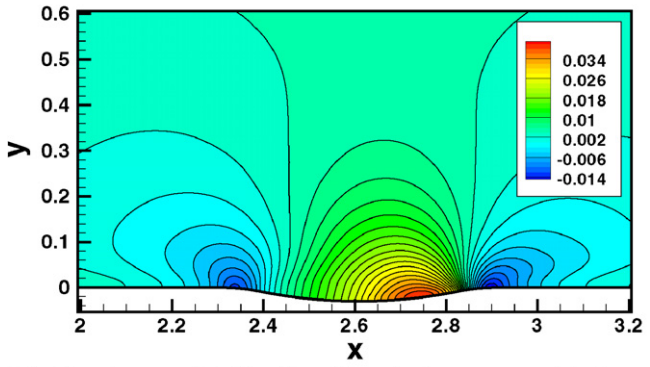

(b) Contours of $\overline{p}$ in the dimple in a x-y midplane

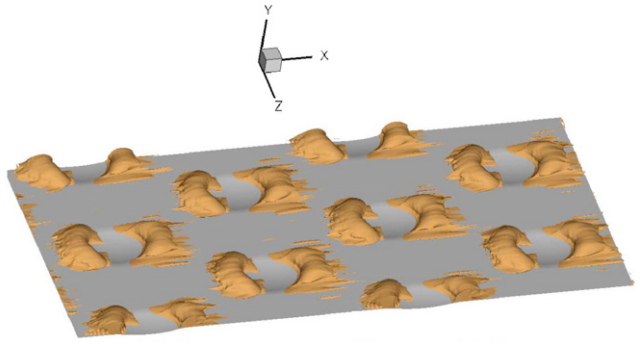

(c) Iso-surfaces of $\lambda_2 = -0.05$

Fig. 12. Channel flow with multiple dimples at both walls, case **B**, fine grid simulation, $Re = 10,935$.

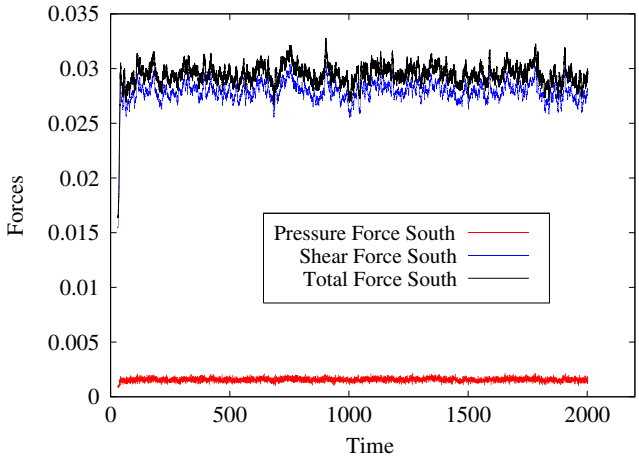

(a) Forces at lower wall with dimples

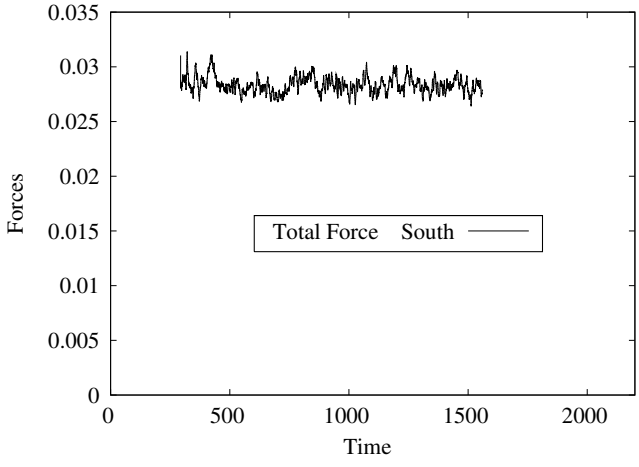

(b) Forces at lower wall without dimples

Fig. 13. History of dimensionless forces (non-dimensionalized by $\rho U_b^2 \delta^2$) at the lower wall for case **B** and case **R**, fine grid simulation, $Re = 10,935$.

Table 3
Integral results for all cases; shear, pressure, and total forces on the dimpled walls in relation to the reference case **R**; resulting skin-friction coefficient C_f and ratio $C_f^{dimple}/C_f^{smooth}$

	Coarse grid			Fine grid	
	L	**B**	**R**	**B**	**R**
Lower wall					
Shear force ratio	98.24%	98.49%	100%	98.59%	100%
Pressure force ratio	5.45%	5.49%	0%	5.54%	0%
Total force ratio	103.69%	103.98%	100%	104.13%	100%
Upper wall					
Shear force ratio	100.21%	98.13%	100%	99.14%	100%
Pressure force ratio	0%	5.45%	0%	5.57%	0%
Total force ratio	100.21%	103.58%	100%	104.71%	100%
Total					
C_f	.00565	.00575	.00554	.00586	.00562
C_f ratio	101.99%	103.79%	100%	104.40%	100%

wall of case **B** and on the non-dimpled smooth wall of case **R**. For the non-dimpled wall the situation is simple, since on this surface only the wall-shear stress leads to a skin-friction drag. This force also acts on the lower dimpled wall, where the time-average is marginally smaller on the dimpled wall than on the smooth wall (see also Table 3). However, at the dimpled wall the pressure distribution on the wavy surface (Fig. 12b) yields a pressure force in the main flow direction (about 5.5% of total force) which contributes to the total drag force. Both effects – the slight decrease of the average shear force and the additional contribution of the pressure force – approximately compensate each other, so that there is no net drag reduction due to the dimples. In fact, the total drag for case **B** even increases about 4.4% compared to the fine grid reference case **R**. For the coarse grid, we found an increase of about 2.0% and 3.8%, respectively for the case **L** (one dimpled wall) and case **B** (two dimpled walls). Thus the effect of the dimples is approximately doubled for case **B** compared with case **L** and an increase of about 4% is found for case **B** on both grids. Hence, these simulations confirm our experimental findings that the present arrangement of dimples does not lead to drag reduction but rather to a slight increase of the total drag.

5. Conclusions

Based on the simulations and the measurements described above, the question whether the present arrangement of dimples leads to drag reduction has to be answered in the negative. That is supported by both experimental measurements of an internal and an external flow as well as DNS of channel flows with dimpled and smooth walls. However, a significant increase of pressure loss was also not observed. Integrated over the entire surface the contribution from the shear stresses is marginally decreased by the shallow dimples but the effect on the drag is overcome by the newly appearing pressure force contribution. This outcome is consistent with an experimental investigation by Zhao et al. (2004) which for a hydraulically smooth channel also observed deviations of the friction coefficient with and without dimples within the margins of the measurement uncertainties. Concerning prospective applications of dimpled surfaces in engineering, this study implies that it is feasible to achieve an augmentation of heat-transfer by shallow dimples without significant additional pressure losses typically encountered with deep dimples.

Acknowledgments

This work was supported by the *Deutsche Forschungsgemeinschaft* under contract number BR 1847/9. The computations were carried out on the NEC SX-8 machine at HLRS Stuttgart (Grant No.: DIMPLE/12760). The dimple geometries were kindly supplied by Inventors Network GmbH. All kinds of support are gratefully acknowledged.

References

Alekseev, V.V., Gachechiladze, I.A., Kiknadze, G.I., Oleinikov, V.G., 1998. Tornado-like energy transfer on three-dimensional concavities of reliefs-structure of self-organizing flow, their visualisation, and surface streamlining mechanisms. In: Transactions of the 2nd Russian Nat. Conf. of Heat Transfer, Heat Transfer Intensification Radiation and Complex Heat Transfer, vol. 6. Publishing House of Moscow Energy Institute (MEI), Moscow, pp. 33–42.

Breuer, M., 1998. Large-eddy simulation of the sub-critical flow past a circular cylinder: numerical and modeling aspects. Int. J. Num. Meth. Fluids 28, 1281–1302.

Breuer, M., 2002. Direkte Numerische Simulation und Large-Eddy Simulation turbulenter Strömungen auf Hochleistungsrechnern, Habilitationsschrift. Univ. Erlangen-Nürnberg, Berichte aus der Strömungstechnik, ISBN: 3-8265-9958-6.

Breuer, M., Rodi, W., 1996. Large-eddy simulation of complex turbulent flows of practical interest. In: Hirschel, E.H. (Ed.), Flow Simulation with High-Performance Computers II, vol. 52. Vieweg Verlag, Braunschweig, pp. 258–274.

Bui, T.T., Oates, D.L., Gonsalez, J.C., 2000. Design and Evaluation of a New Boundary-layer Rake for Flight Testing, NASA/TM-2000-209014.

Burgess, N.K., Oliveira, M.M., Ligrani, P.M., 2003. Nusselt number behavior on deep dimpled surfaces within a channel. J. Heat Transfer 125, 11–18.

Dean, R.B., 1978. Reynolds number dependence of skin friction and other bulk flow variables in two-dimensional rectangular duct flow. J. Fluids Eng. 100, 215–223.

Jeong, J., Hussain, F., 1995. On the identification of a vortex. J. Fluid Mech. 285, 69–94.

Moser, R.D., Kim, J., Mansour, N.N., 1999. Direct numerical simulation of turbulent channel flow up to $Re_\tau = 590$. Phys. Fluids A 11 (4), 943–945.

Zhao, J.B., Chew, Y.T, Khoo. B.C., 2004. Experimental studies on hydrodynamic resistance and flow pattern of a narrow flow channel with dimples on the wall. In: Proc. ASME Int. Mech. Eng. Congress and Exhibition, Anaheim, CA, USA, Nov. 13–20, IMECE2004–59506.